Proceedings of IMECE2005
2005 ASME International Mechanical Engineering Congress and Exposition
November 5-11, 2005, Orlando, Florida USA

IMECE2005-82158

DESIGN AND MODELING OF THERMALLY ACTUATED MEMS NANOPOSITIONERS

Sébastien Bergna, Jason J. Gorman* and Nicholas G. Dagalakis
Intelligent Systems Division
National Institute of Standards and Technology
Gaithersburg, Maryland 20899-8230
*contact author: gorman@nist.gov

ABSTRACT

Several micro-scale nanopositioning mechanisms, or MEMS nanopositioners, have been developed for application in nanotechnology and optical sensors. In this paper, the design and modeling of these devices is presented along with initial experimental results. The MEMS nanopositioner is comprised of a parallel bi-lever flexure mechanism and a bent-beam thermal actuator. The flexure mechanism is designed to amplify and guide the motion of the actuator with high precision, while the thermal actuator provides the necessary force and displacement. The relationship between the applied voltage and resulting displacement for this mechanism has been calibrated using a scanning electron microscope and a simple image processing technique. A finite difference thermal model along with a FEA representation of the flexure mechanism and actuator is used to estimate the motion range of the device. Results from this method are compared with experimental calibrations, showing that the model provides a sufficient approach to predict the mechanism's static performance. Finally, an open-loop controller based on calibration data was used to demonstrate the nanopositioning capabilities of these devices. The motion repeatability was found to be less than +/- 7 nm and step sizes well below 50 nm are possible, indicating suitable performance for many nanopositioning applications.

Keywords: nanopositioning, MEMS, thermal actuator

INTRODUCTION

Nanopositioning mechanisms have been used extensively in high precision positioning applications such as scanning probe microscopy (SPM), laser beam alignment and steering, and micromanipulation. Although these mechanisms provide nanometer-scale positioning resolution and accuracy, they are limited by two factors in particular: 1) their macro-scale dimensions, and 2) their high cost. Both of these factors prohibit the highly parallel nano-scale manipulation and assembly strategies which have been a major focus of nanotechnology research. In this paper, the design and modeling of a microelectromechanical system (MEMS) developed specifically for nanopositioning will be discussed. This research aims to eventually create MEMS nanopositioners which meet or exceed the positioning performance of their macro-scale counterparts.

MEMS nanopositioners can be used in many of the applications found by macro-scale mechanisms. Additionally, new opportunities arise due to their low cost, small size, increased bandwidth, highly parallel operation capabilities, and possible integration with nanofabrication processes. One example is a micro-scale scanning probe microscope (SPM), as developed by Xu et al. [1]. The miniaturization of an SPM provides the opportunity to image larger surface areas in shorter time by using an array of devices. Another application is scanning laser arrays such as those used in optical communications. Tuantranont et al. [2] have developed large arrays of *x-y* microlens scanners coupled with VCSELs. Eleftheriou et al. [3] have used MEMS nanopositioners in the development of high density data storage devices, taking full advantage of the size, cost, and precision provided by such mechanisms.

Multi-degree-of-freedom micro-scale motion stages have been developed for many years [4]. However, recently there has been more emphasis on designing stages with higher precision in terms of motion repeatability and positioning resolution. Examples include a silicon-on-insulator (SOI) *x-y* stage with electrostatic actuators [5], a 2 degree-of-freedom (DOF) thermal actuation scheme that includes sub-nanometer position sensing [6], and a closed-loop controlled 1 DOF stage with an electrostatic actuator and capacitive sensor [7]. In several cases, nanometer-scale positioning resolution has been demonstrated to some degree. Hoen et al. [8] have shown that an electrostatic surface drive can be driven to move in a 1 nm square wave by toggling the least significant bit of the drive voltage. Nano-scale resolution was also demonstrated for a stress-strain device designed to test the mechanical properties of nanomaterials. Finally, Hubbard and Howell [10] recently presented nanopositioning repeatability and resolution results for surface micromachined bent-beam thermal actuators.

Although these advances demonstrate the possibilities for MEMS nanopositioners, further research is required to yield reliable and repeatable devices that can perform as well as macro-scale nanopositioners.

The objective of this paper is to present two MEMS nanopositioner designs (1 DOF and 2 DOF) along with initial experimental performance results. These mechanisms were based on a previously developed high-precision flexure mechanism used in macro-scale nanopositioners. By scaling down this design and replacing the standard macro-scale piezoelectric actuator with a thermal actuator, it is believed that the high-precision previously demonstrated can be maintained at the micro-scale. A description of these mechanisms will be given in the following section. Then, experimental characterization results for the relationship between the input voltage and output displacement of this device will be presented. A finite-difference model, combining the electrothermal dynamics and a structural FEA of the mechanism, has been used to estimate this relationship. These results are then compared to experimental data. Finally, an open-loop control approach has been used to demonstrate the nanopositioning capabilities of these devices. Multi-step positioning results that provide preliminary estimates of the motion repeatability and resolution of a 1 DOF mechanism are discussed.

MEMS NANOPOSITIONER DESIGN

There have been significant efforts to develop macro-scale nanopositioners that exhibit extremely high positioning precision. Some of the critical parameters which determine the nanopositioner performance are positioning range, resolution, accuracy, and bandwidth. Another important set of criteria are the parasitic errors of the mechanism. These are undesirable motions such as cross-talk between orthogonal axes and rotational motion of the stage. The performance requirements vary drastically from application to application. However, in general, it is typical to try to maximize the ratio of range over resolution, along with the bandwidth, while minimizing parasitic errors, and the motion resolution. In this section, the design of micro-scale nanopositioning mechanisms, or MEMS nanopositioners, based on a high-precision macro-scale nanopositioner design will be discussed.

A number of MEMS nanopositioners have been designed and fabricated with various configurations of geometric parameters. These include 1 DOF and 2 DOF nanopositioners, such as those shown in Fig. 1 and Fig. 2, respectively. Each axis of motion for these mechanisms is composed of two subcomponents, a flexure mechanism and a thermal actuator. The flexure mechanism design is based on the parallel bi-lever flexure mechanism that has been used in macro-scale nanopositioners [11]. The thermal actuator is similar to the bent-beam design discussed by Que et al. [12].

The basic layout of the parallel bi-lever flexure mechanism is described in Fig. 3. The mechanism is comprised of an actuator input stage, four lever arms, ten circular flexure hinges (numbered 1-10), and an output stage. Each flexure hinge provides a point of compliance and acts similar to a rotational joint with an attached rotational spring. A close-up of flexures 1 and 2 is shown in Fig. 4. The actuator input stage, lever arms and output stage are connected through the flexure hinges. These components are significantly stiffer than the flexure

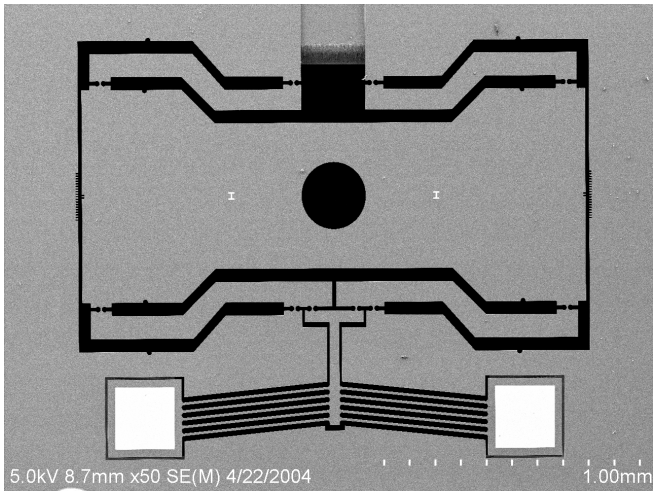

Fig. 1 One DOF MEMS nanopositioner (SEM image)

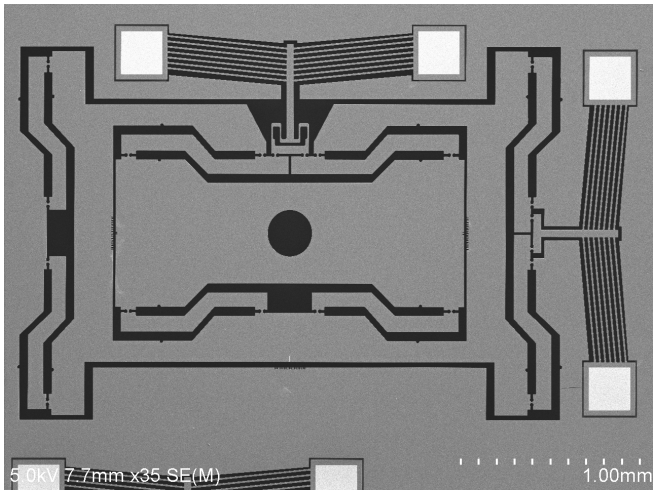

Fig. 2 Two DOF MEMS nanopositioner (SEM image)

hinges, such that they act as rigid bodies in the plane of motion. Therefore, the device is an overconstrained parallel mechanism that can only move due to flexure hinge compliance. A force applied at the actuator input causes the bottom two levers to rotate about their center flexure hinges (flexures 2 and 9), which are rigidly grounded to the supporting substrate. These lever arms then transmit the force directly to the output stage, causing it to move in the opposite direction of the actuator input. In addition to transmitting the actuator force to the output stage, the lever arms amplify or attenuate this motion. The motion gain ratio is b/a where a and b are length segments of the lever arm as indicated in Fig. 3.

The ability to easily amplify or attenuate the motion of the actuator is one advantage of this mechanism design. More importantly, the levers are arranged symmetrically causing a direct cancellation of parasitic motion orthogonal to the actuator. A single lever transmission, as found in many other flexure mechanisms, would result in cross-talk between the x and y axes as well as rotation of the output stage in the plane. This is avoided here since the four levers counterbalance each other such that the output stage motion is along a straight line. Small parasitic errors are inevitable due to fabrication tolerances, causing mismatches in the lever lengths and flexure

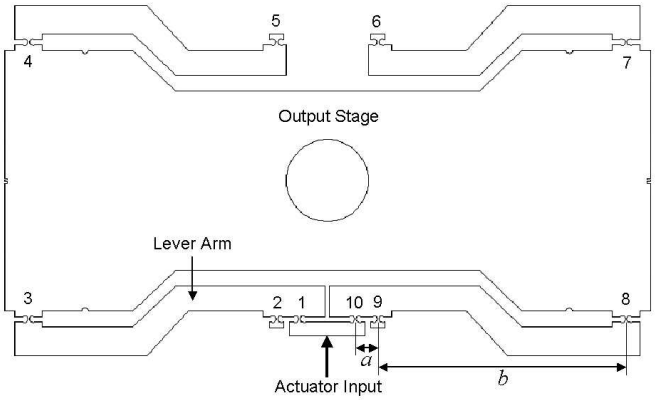

Fig. 3 Parallel bi-lever flexure mechanism layout

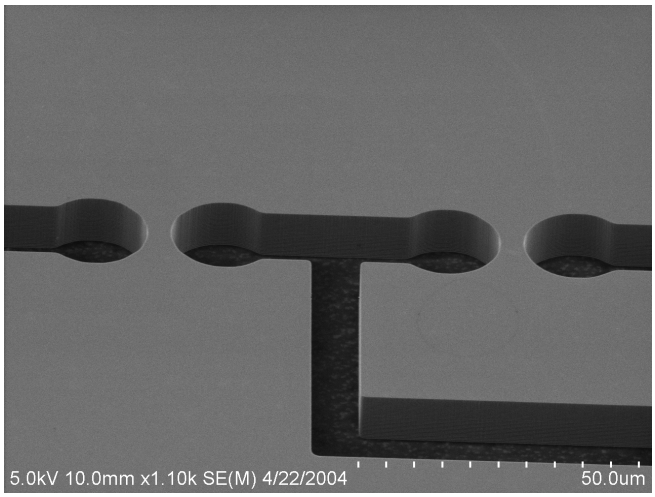

Fig. 4 Circular flexure hinges (SEM image)

parameters. However, these errors have been shown to be extremely small at the macro-scale [11].

The design of multi-degree-of-freedom mechanisms is very challenging due to interactions between DOF. The 2 DOF nanopositioner shown in Fig. 2 uses a so-called *nested* configuration, in which the flexure mechanism for the *y* direction is located inside the mechanism for the *x* direction. In the macro-scale version of this mechanism, the actuator for the *y* direction also fits within the mechanism for the *x* direction. However, this becomes difficult to mimic at the micro-scale, largely due to limitations in fabrication processes and the need to wire bond to a moving portion of the mechanism, possibly constraining it and increasing the chances of an electrical short. Therefore, although a nested design has been used, both of the actuators sit on the outside of the flexure mechanism. In order to decouple the *x* and *y* axes, a double parallelogram flexure was used (see Fig. 5) [13]. The double parallelogram flexure allows force to be transmitted in the *y* direction and reduces the moment on the actuator caused by motion in the *x* direction. This flexure will not provide pure decoupling but it is expected to perform significantly better than a system without it. Other decoupling mechanisms are also currently being pursued.

Bent-beam thermal actuators have been used due to their high force output, straight-line motion, low voltage requirements and ease of micromachining. The force generated by a thermal actuator is significantly larger than that of an

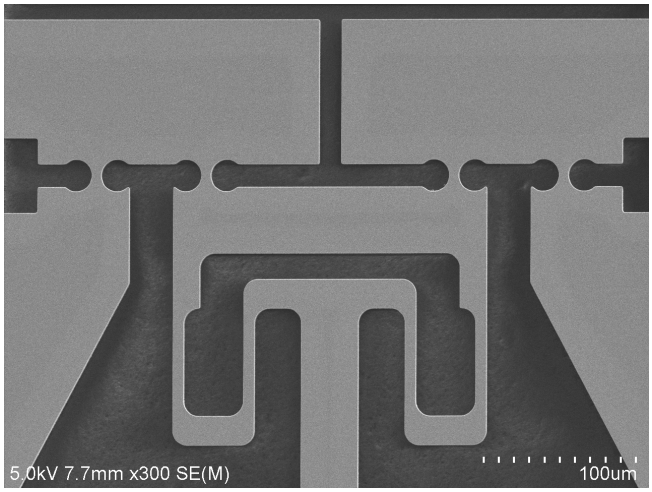

Fig. 5 Double parallelogram flexure for axes decoupling

electrostatic actuator of comparable size [10]. In addition, the control voltage is an order of magnitude smaller than in electrostatic devices. However, one major concern is the effect that the thermal actuator will have on the precision of the stage. Thermal gradients may result in undesirable thermal expansions throughout the device. These problems have yet to be investigated but will be important in later stages of development.

The mechanisms were fabricated through the SOIMUMPs service provided by MEMSCAP[1]. This fabrication process is well documented so it will not be reviewed here [14]. The resulting chips have an n-doped single crystal silicon device layer that is 10 μm or 25 μm thick. The device layer sits on top of a 1 μm silicon oxide layer which subsequently resides on a 400 μm thick insulating substrate. A Cr/Au layer has been deposited on the device layer to form bond pads. For the remainder of the paper, discussions will focus on the 1 DOF mechanism shown in Fig. 1. In the next section, calibration results that relate the output stage displacement to input voltage will be presented.

EXPERIMENTAL CHARACTERIZATION

An important step in modeling these mechanisms is to determine the steady-state relationship between an applied voltage and the displacement of the output stage. Applying a voltage across the bond pads of the thermal actuator causes Joule heating in the thermal actuator, where in this case the resistance is approximately 400 Ω. The resulting thermal expansion of the actuator beams causes the center shuttle to move forward and push on the flexure mechanism. Based on Joule's Law, the output stage displacement is expected to be proportional to the square of the applied voltage, $y \propto V^2$.

The motion of the mechanism has been measured using a scanning electron microscope (SEM) and an optical microscope (OM) to take images of the mechanism for incremental changes in the applied voltage. The motion was captured by focusing

[1]Certain commercial products and processes are identified in this paper to foster understanding. Such identification does not imply recommendation or endorsement by the National Institute of Standards and Technology, nor does it imply that the products and processes identified are necessarily the best available for the purpose.

on a leading edge of the output stage. Image processing was then applied to extract the displacement of that edge for a given voltage. A thresholding algorithm is used to transform the grey-scale image into black and white, highlighting the edge that is being tracked. Then a simple search and averaging algorithm calculates the relative displacement from image to image. The pixel resolution for these tests was 167 nm for the OM (140X mag.) and 6.5 nm for the SEM (8kX mag.).

This approach was applied to two different 1 DOF MEMS nanopositioners with 10 μm and 25 μm thick device layers, respectively. The results from SEM and OM tests, as shown in Figs. 6-7, indicate that the nanopositioner motion is in fact quadratic with respect to the applied voltage. One can also see that the nanopositioner moves farther in vacuum (SEM) than in air (OM) for the same applied voltage. This is expected since conduction and convection are not efficient methods of heat transfer in vacuum, resulting in higher actuator temperatures, and therefore, additional thermal expansion. It is also clear that the increased device thickness drastically reduces the motion range of the stage. At 6 V, the 10 μm thick device moves 2.5 times more than the 25 μm thick device.

The reduction in motion caused by the increased device layer thickness is due to a number of factors. First, the stiffness of the circular flexure hinges, and therefore the flexure mechanism, is proportional to $L_{Si}^{5/2}$ [13] where L_{Si} is the thickness of the device layer. In contrast, the stiffness of the thermal actuator is directly proportional to L_{Si} based on beam theory. Therefore, as the thickness increases the ratio of the respective stiffnesses for the flexure mechanism and actuator changes nonlinearly and the transmission of motion becomes less efficient. The larger thickness also causes a higher temperature gradient across the layer because the structure can dissipate heat more efficiently due to the increased surface area. Finally, the doping profile in the device layer is believed to be 3 to 5 μm deep regardless of the device layer thickness. Therefore, as the thickness increases the ratio between the conducting and insulating layers decreases causing heterogeneous heating across the structure.

In many applications it is desirable to manufacture very rigid structures so that they are robust to external forces and can support reasonable loads. However, it is clear from these results that smaller, thinner mechanisms can more readily achieve high displacements. The flexure mechanism and actuator designs will be optimized in future fabrication runs so that high stiffness and long range can be achieved simultaneously.

NANOPOSITIONER MODELING

Due to the complex relationship between the nanopositioner geometry and the resulting displacement range, a numerical method for estimating the range for a given device is needed. This method could be used to simply verify designs or to optimize the relative compliance between the actuator and flexure mechanism. Lott et al. [15] have developed a finite difference approach for modeling the thermal behavior of surface-micromachined thermal actuators. In this section, the finite difference approach is applied to the SOI thermal actuators discussed in this paper. The model presented in [15] only provides a method for determining the thermal actuator

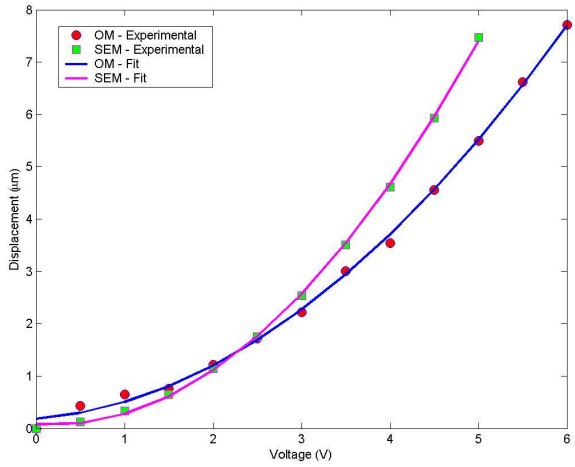

Fig. 6 Experimental displacement vs. applied voltage results for 10 μm thick device (SEM and OM tests)

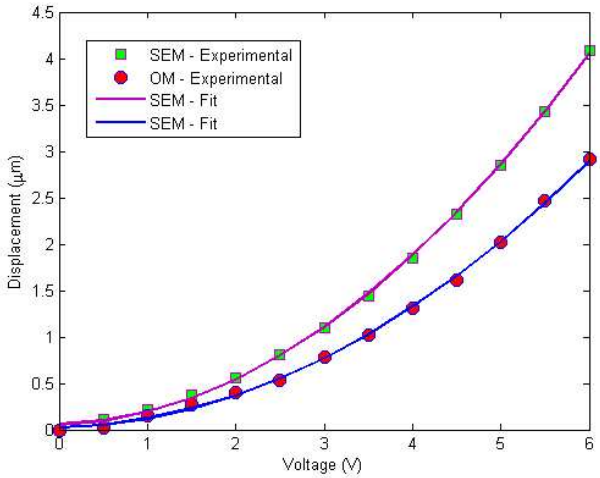

Fig. 7 Experimental displacement vs. applied voltage results for 25 μm thick device (SEM and OM tests)

motion for a given voltage. However, in our case, the displacement is also a function of the compliance of the flexure mechanism and actuator. Therefore, FEA has been used to determine the stiffnesses of the sub-components and then this is combined with the thermal actuator model to estimate the displacement of the output stage.

There are a few significant differences between surface micromachined thermal actuators and those fabricated using a SOI process. First, in the SOIMUMPs process there is a large gap between the SOI actuator and chip package, on the order of 400 μm. Conversely, surface micromachined actuators are very close to the substrate, with only a few micrometers between the two. Therefore, heat transfer by free convection will have a much larger effect in SOI systems than in those that are surface micromachined. Similarly, conduction to the substrate is far less significant in SOI actuators for the same reason. The finite difference approach has been modified to address these issues. However, the method is still very similar to the presentation by Lott et al. [15]. In the following development, the basic equations for the method are presented and the modifications

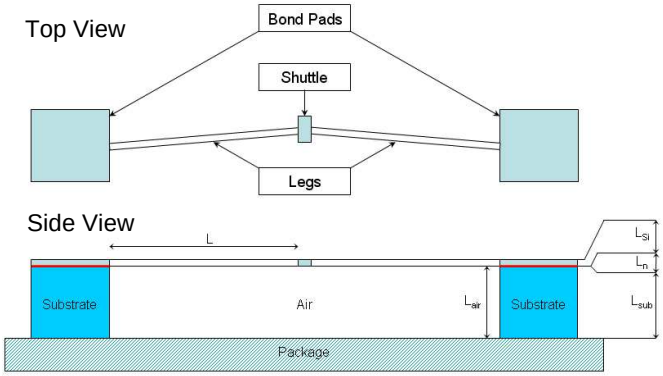

Fig. 8 Bent-beam thermal actuator cross-section

are highlighted. However, readers should see [15] for the details of this approach.

A simplified SOI thermal actuator is shown in Fig. 8. As in [15], the following 1-D thermal model will be derived for a single leg of the thermal actuator without any loss of generality. The leg is divided into *N* segments and an energy balance is derived across each element. The result of the energy balance across the *i*th element is:

$$q_\Omega + q_{cond} + q_{rad} + q_{cond,i-1} + q_{cond,i+1} + q_{conv} = q_{st} \tag{1}$$

where q_Ω is the rate of energy due to Joule heating, q_{cond} represents conduction to the substrate, $q_{cond,i-1}$ and $q_{cond,i+1}$ model the conduction between adjacent elements, q_{conv} represents free convection, and q_{st} is the rate of change of stored energy within an element. The only term in Eq. (1) that does not appear in the energy balance presented in [15] is q_{conv}. This has been added to account for the large gap between the device layer and chip package. Heat transfer by natural convection from a solid to a surrounding fluid can be described by Newton's law of cooling [16]:

$$q_{conv} = hA_c[T_{sur} - T_i(j)] \tag{2}$$

where $T_i(j)$ is the temperature of the *i*th element of the actuator leg at the *j*th time step, T_{sur} is the temperature of the surrounding air, A_c is the heat transfer surface area and *h* is the average heat transfer coefficient on the surface. All of the other terms in Eq. (1) are described in [15] and are omitted here. Substituting all of these terms into Eq. (1) and solving for the temperature at the (*j*+1)th time step results in the following:

$$\begin{aligned} T_i(j+1) = \frac{\Delta t}{\rho c \Delta V_i}\Big[J^2(j)\rho_r \Delta V_i + \frac{SA_u}{G_u}\left(T_{pack} - T_i(j)\right) \\ + \varepsilon\sigma A_s\left(T_{sur}^4 - T_i^4(j)\right) + \frac{k_{Si}A_x}{\Delta x}\left(T_{i-1}(j) - T_i(j)\right) \\ + \frac{k_{Si}A_x}{\Delta x}\left(T_{i+1}(j) - T_i(j)\right) + h A_c\left(T_{sur} - T_i(j)\right)\Big] \\ + T_i(j) \end{aligned} \tag{3}$$

The parameter Δt is the simulation time step, ρ is the density of single crystal silicon (SCS), *c* is the specific heat of SCS, ΔV_i is the element volume, *J* is the current density, ρ_r is the resistivity of SCS, A_u is the surface area of the side of the element that faces the package, T_{pack} is the package temperature, A_s is the surface area where radiation occurs, ε is the emissivity of the surface, σ is the Stefan-Boltzmann constant, k_{Si} is the thermal conductivity of SCS, A_x is the cross-sectional area of an element, and Δx is the length of an element. The shape factor, *S*, is described as:

$$S = \frac{L_{Si}}{w}\left(\frac{2L_{air}}{L_{Si}} + 1\right) + 1 \tag{4}$$

where L_{Si} is the height of the element, *w* is the width of the element, and L_{air} is the gap between the bottom of the device layer and the chip package.

The heat path for conduction in SOI thermal actuators is different than for the silicon micromachined actuators described in [15]. The serial heat path for all of the layers can be written as:

$$G_u = \frac{L_{air}}{k_{air}} + \frac{L_{SiO_2}}{k_{SiO_2}} + \frac{L_{sub}}{k_{sub}} \tag{5}$$

where L_{SiO_2} is the silicon oxide layer thickness, L_{sub} is the substrate thickness, and k_{air}, k_{SiO_2}, and k_{sub} are the thermal conductivities for their respective layers. There are two distinct regions, the area beneath the actuator legs and the area underneath the bond pads. Underneath the legs, the silicon oxide and substrate layers are not present so L_{SiO_2} and L_{sub} are set equal to zero. Similarly, the air layer is not present under the bond pads and L_{air} is therefore set equal to zero in that region.

The spatial temperature distribution along the actuator length can be calculated for a given applied voltage by implementing Eq. (3) for all elements over time. Simulations were performed for a SOI thermal actuator with similar dimensions as the one shown in Fig. 1. Independent thermal actuators were fabricated in addition to the MEMS nanopositioners. The objective of these simulations is to accurately model the displacement of an independent thermal actuator. These results can then be combined with FEA, which will be discussed shortly.

As in [15], many of the model parameters are temperature dependent and appropriate functions for these parameters have been included in the simulations, including k_{air}, k_{Si}, and *c*. The boundary conditions are chosen such that T_{pack} and T_{sur} are constant and equal to 20°C. The actuator was divided into 184 elements and the simulation time step, Δt, was chosen to be 1 μs to maintain simulation stability. The simulation was implemented for a voltage range of 0 to 12 V.

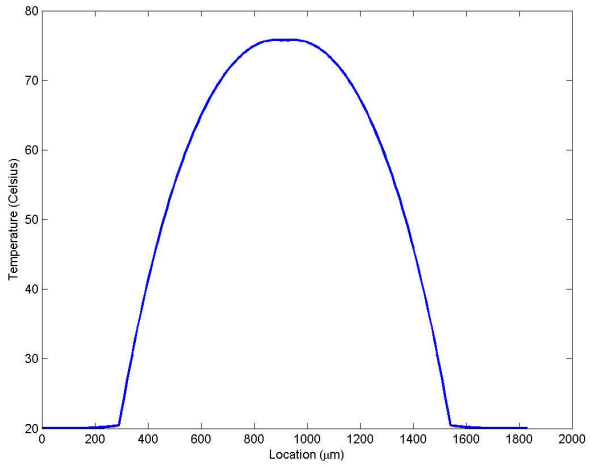

Fig. 9 Simulated temperature profile for a 10 μm thick thermal actuator with a 5 V input voltage

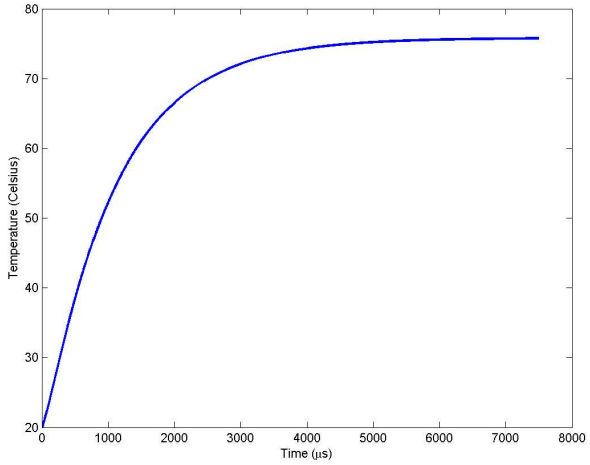

Fig. 10 Simulated step response for a 10 μm thick thermal actuator with a 5 V input voltage

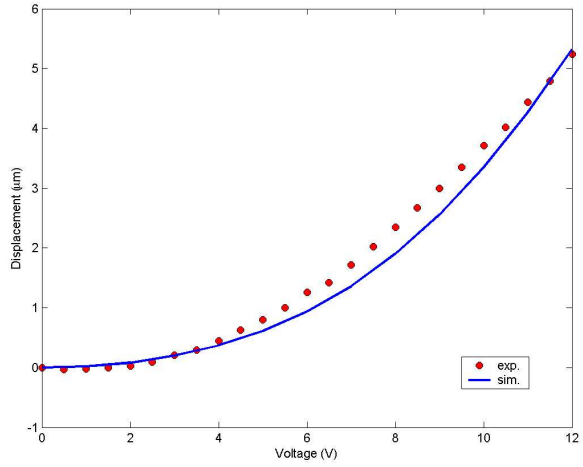

Fig. 11 Experimental and simulated displacement vs. applied voltage results for a 10 μm thick thermal actuator

The temperature distribution for a 5 V input voltage is shown in Fig. 9 and the temperature convergence over time for the center element is shown in Fig. 10. The temperature distribution is then applied to a simple finite element representation of thermal expansion of the actuator. The simulated and experimental displacement results for a thermal actuator which is not attached to a flexure mechanism is shown in Fig. 11. These results show a strong correlation between the model and experimental data.

As a first-pass at developing a static model of the displacement of the MEMS nanopositioner for given input voltages, we combined structural FEA with the finite-difference thermal model. The finite-difference model is used to simulate the displacement of the thermal actuator, while the FEA provides information on the mechanical coupling between the flexure mechanism and the actuator, as well as the motion amplification ratio between the input stage and the output stage (Fig. 12). The FEA for this particular example determined that the thermal actuator motion is amplified by a factor of 6.5 at the output stage.

The complete static model for the MEMS nanopositioner is found by applying this transmission ratio to the displacement results previously found using the thermal actuator simulation. In Fig. 13, the model and experimental results for the MEMS nanopositioner are shown. For low voltages, the model accurately predicts the displacement of the stage. However, at higher voltages, the experimental stage motion results reach a plateau while the model continues on a quadratic trend. These experimental results are not fully understood but it is believed that the flexure mechanism and/or the actuator begins to buckle at higher voltages. Mechanisms with a thicker device layer have not exhibited this behavior, so out-of-plane motion is a likely cause. Regardless, the combined finite difference and FEA approach appears to be a suitable method for estimating the displacement range for the MEMS nanopositioners

OPEN-LOOP POSITIONING

The ability of a micro-scale mechanism to accurately track desired positions without the need for a position feedback sensor is an important attribute. This is due to the fact that feedback can often result in a degradation of positioning resolution caused by sensor noise. Furthermore, many MEMS applications will require open-loop operation in order to avoid complex control system electronics. Although position sensors will be added in subsequent designs, it is important to look at the nanopositioning capabilities of these devices without the use of feedback. In this section, initial results on the motion repeatability and resolution will be presented.

Several nanopositioning results at the micro-scale were mentioned earlier [8]-[10]. In all of these cases, the nano-scale positioning results that were presented were generated by applying very small changes in either the drive voltage or current. Rather than commanding the stage to a desired position, the input was simply changed to show some small motion that was not specified *a priori*. A better approach is to apply an open-loop controller that calculates the required voltage to drive the nanopositioner to a desired position.

Such an open-loop controller has been implemented on the 1 DOF MEMS nanopositioner. There are a number of methods for implementing such a controller, based on either a static or dynamic model of the system. Since an accurate dynamic

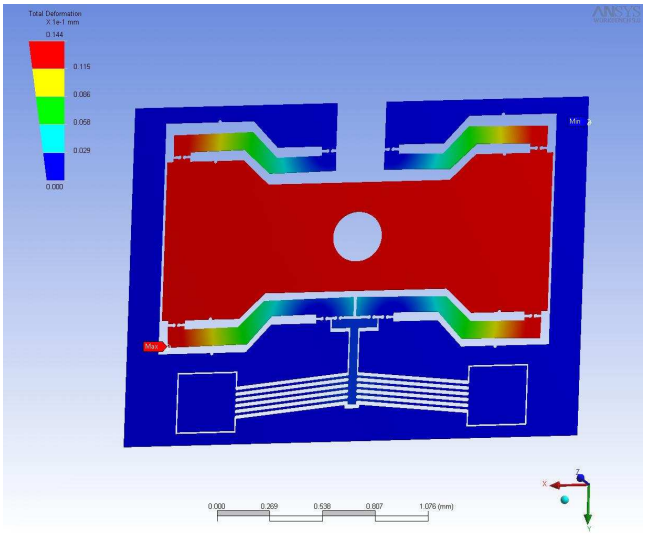

Fig. 12 FEA analysis showing displacement distribution for a 10 μm thick MEMS nanopositioner

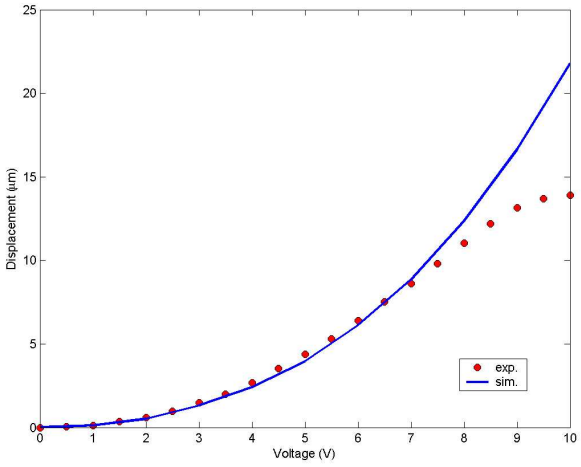

Fig. 13 Experimental and simulated displacement vs. applied voltage results for a 10 μm thick MEMS nanopositioner

model has yet to be developed, a simple open-loop controller was used to demonstrate the concept. A quadratic least-squares fit was applied to the calibration data shown in Fig. 7. Then the resulting equation was solved in terms of the voltage, choosing the positive valued solution. Therefore, a value for the voltage can be calculated based on the desired position.

This controller was applied to the mechanism using data acquisition and control hardware and software on a PC. An analog output PCI card was connected to an op-amp circuit to increase the available power, and the output of the op-amp was connected to the nanopositioner while in an SEM via a feedthrough port. A control interface was developed to generate desired position trajectories, which in this case consist of steps of different amplitude, and to calculate the required control voltage.

The SEM was used to measure the response of the mechanism using similar image processing techniques as mentioned previously. However, instead of taking still images, as we did in the displacement – voltage characterization, a SEM video signal at a rate of 30 frames per second was captured using a video digitizer attached to a PC. This facilitated the measurement of the stage displacement as a function of time. One disadvantage of this approach is that the SEM images contain more noise due to the lack of averaging in video mode. Additionally, the number of pixels in each image was reduced by a factor of 16. Although a magnification of 20kX and 45kX was used in the following two experiments respectively, the associated pixel resolution was 9.4 nm and 4.4 nm. Therefore, the imaging resolution is on the same level as used in the static calibrations although the signal-to-noise ratio is worse in this case.

The first experiment was designed to test the motion repeatability and short term drift. The nanopositioner was driven to perform 1 μm steps over a 3 μm range. The results of this test are shown in Fig. 14. A number of performance parameters can be derived from this set of data. First, it was found that for larger excursions from zero, the position accuracy decreases. The accuracy for a desired position of zero was 6nm and for 3 μm it was 120 nm. Additionally, the accuracy was found to be 13 nm and 32 nm for the intermediate steps. This phenomena is likely due to errors in the calibration curve fit.

The repeatability was also calculated by first taking the average position at each step size and then determining the maximum error when returning to a particular step. Due to the chosen trajectory, bi-directional repeatability can be determined for the steps at 1 μm and 2 μm, and uni-directional repeatability for 0 μm and 3 μm. The repeatability in all cases was bounded by +/-7 nm. Finally, a drift in position was detected on the order of 6 nm over 20 s. This may be related to the MEMS nanopositioner but it is more likely related to the SEM sample stage.

The second experiment was designed to demonstrate controlled repeatable motions near the nanometer level. A step size of 50 nm was chosen so that the motion was easily distinguishable from the noise attributed to the SEM video and image processing. Fig. 15 shows the nanopositioner motion when commanded in 50 nm steps. The main limitation for the position resolution is the measurement noise, which in this case is approximately +/-12 nm. Steps below this would be difficult to visualize as a function of time. However, high-resolution imaging using averaging of the SEM signal could provide better results but at slower frame rates. Based on these results, the open-loop control approach has proved to be very effective and it is likely that the performance can be further improved by a more rigorous calibration and curve fitting procedure. Additionally, nanometer resolution appears to be possible but is largely dependent on the development of a suitable sensor that can be integrated into the system.

CONCLUSION

A new class of MEMS nanopositioners that combine a parallel bi-lever flexure mechanism with a bent-beam thermal actuator has been introduced. The advantages of this design have been presented along with details on 1 and 2 DOF mechanisms. The steady-state relationship between displacement and applied voltage for two 1 DOF mechanisms has been characterized by using optical and scanning electron microscopes coupled with an image processing algorithm. The

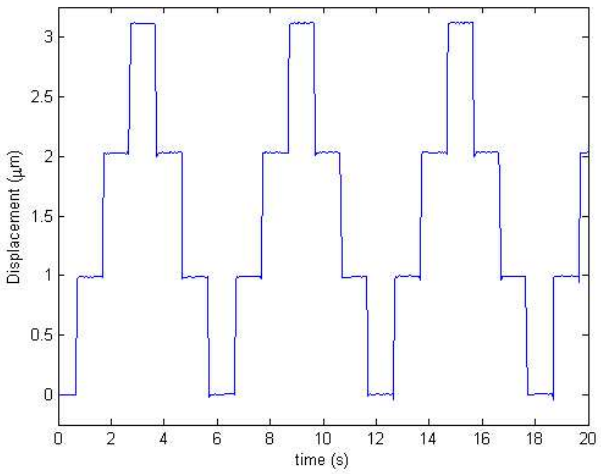

Fig. 14 Open-loop controlled 1 μm steps

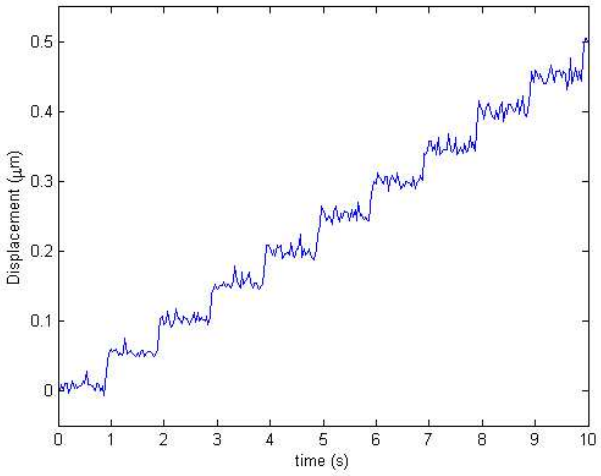

Fig. 15 Open-loop controlled 50 nm steps

displacement - voltage relationship was found to be strongly quadratic and the maximum displacement for both nanopositioners was approximately 12 μm. Based on these results a finite difference model was used to estimate the temperature distribution in the thermal actuator. The thermal expansion of the actuator could then be calculated and the motion of the output stage was estimated based on the motion transmission efficiency determined by FEA. The model results were shown to provide a reasonable approximation of the output stage motion and will be used in the future to optimize the design of the flexure mechanism and actuator for longer travel. The nanopositioning capabilities of the mechanism were also demonstrated. An open-loop controller that inverts the displacement – voltage calibration was used to move in 1 μm and 50 nm steps. The repeatability for these steps was +/-7 nm and the position resolution appears to be 12 nm or less.

REFERENCES

[1] Xu, Y., MacDonald, N. C., and Miller, S. A., 1995, "Integrated micro-scanning tunneling microscope," *Applied Physics Letters*, **67**, pp. 2305-2307.

[2] Tuantranont, A. et al., 2001, "Optical beam steering using MEMS-controllable microlens array," *Sensors and Actuators A*, **91**, pp. 363-372.

[3] Eleftheriou, E. et al., 2003, "Millipede - A MEMS-based scanning-probe data-storage system," *IEEE Transactions on Magnetics*, **39**, pp. 938-945.

[4] Jaecklin, V. P., Linder, C., de Rooij, N. F., and Moret, J. M., 1992, "Micromechanical comb actuators with low driving voltage," *Journal of Micromechanics and Microengineering*, **2**, pp. 250-255.

[5] Kim, C.-H. and Kim, Y.-K., 2002, "Micro XY-stage using silicon on a glass substrate," *Journal of Micromechanics and Microengineering*, **12**, pp. 103-107.

[6] Chu, L. L. and Gianchandani, Y. B., 2003, "A micromachined 2D positioner with electrothermal actuation and sub-nanometer capacitive sensing," *Journal of Micromechanics and Microengineering*, **13**, pp. 279-285.

[7] Horsley, D. A., Wongkomet, N., Horowitz, R., and Pisano, A. P., 1999, "Precision positioning using a microfabricated electrostatic actuator," *IEEE Transactions on Magnetics*, **35**, pp. 993-999.

[8] Hoen, S. et al., 2003, "A high-performance dipole surface drive for large travel and force," *Proceedings of Transducers '03*, Boston, MA, pp. 344-347.

[9] Lu, S. et al., 2004, "Realization of nanoscale resolution with a micromachined thermally actuated testing stage," *Review of Scientific Instruments*, **75**, pp. 2154-2162.

[10] Hubbard, N. B. and Howell, L. L., 2005, "Design and characterization of a dual-stage, thermally actuated nanopositioner," *Journal of Micromechanics and Microengineering*, **15**, pp. 1482-1493.

[11] Dagalakis, N. G., Kramar, J. A., Amatucci, E., & Bunch, R., 2001, "Kinematic modeling and analysis of a planar micro-positioner", *Proceedings of the ASPE Annual Meeting*, Crystal City, VA, pp. 135-138.

[12] Que, L., Park, J.-S., and Gianchandani, Y. B., 2001, "Bent-beam electrothermal actuators – Part I: Single beam and cascaded devices," *Journal of Microelectromechanical Systems*, **10**, pp. 247-254.

[13] Smith, S. T., 2000, *Flexures: elements of elastic mechanisms*, Gordon and Breach: Amsterdam.

[14] Miller, K., Cowen, A., Hames, G., and Hardy, B., 2004, "SOIMUMPs design handbook," MEMSCAP.

[15] Lott, C. D., McLain, T. W., Harb, J. N., and Howell, L. L., 2002, "Modeling the thermal behavior of a surface-micromachined linear-displacement thermomechanical microactuator," *Sensors and Actuators A*, **101**, pp. 239-250.

[16] Holman, J. P., 1990, *Heat Transfer*, McGraw-Hill: New York.

[17] INSPEC, 1988, *Properties of Silicon*, IEE: London.